Nanoscale

PAPER

View Article Online
View Journal | View Issue

Cite this: *Nanoscale*, 2025, **17**, 22226

Defect engineering and hydrogen-induced reversibility in metallic states of MoS_2 grain boundaries

Hangbo Zhou, *[a] Viacheslav Sorkin, [a] ZhiGen Yu, [a] Kah-Wee Ang[b,c] and Yong-Wei Zhang *[a]

One-dimensional metallic states along grain boundaries (GBs) in two-dimensional (2D) semiconducting materials offer unique opportunities for electronic and quantum device applications. However, the stability and tunability of these metallic states remain poorly understood. Here, we systematically investigate how point defects and hydrogenation affect the electronic properties of representative GBs in monolayer MoS_2 using density functional theory. We identify two classes of GBs based on their symmetry response to point defects: defect-sensitive boundaries, which lose metallic states due to symmetry breaking, and defect-robust boundaries, which preserve metallic conduction owing to symmetry retention. Remarkably, hydrogenation can reverse the effects of point defects, restoring metallic states in defect-sensitive GBs and opening band gaps in defect-robust ones. These findings reveal a reversible and controllable mechanism for tuning grain boundary conduction through defect engineering and chemical functionalization, offering new pathways for nanoscale interconnects and reconfigurable 2D electronic devices.

Received 27th May 2025,
Accepted 14th August 2025

DOI: 10.1039/d5nr02232k

rsc.li/nanoscale

Introduction

Grain boundaries (GBs) are intrinsic to large-area semiconducting 2D materials—such as transition metal dichalcogenides (TMDCs), phosphorene, and others—synthesized by chemical vapour deposition. They play a critical role in determining the physical behaviour of these materials.[1–4] These extended line defects originate from the coalescence of misoriented crystalline domains and significantly influence key material properties, including charge carrier mobility, thermal transport, chemical reactivity, and mechanical strength.[5–11] Beyond acting as scattering centres or recombination sites, GBs can also introduce new structural symmetries and electronic states that are absent in the domain lattice, enabling emergent functionalities not accessible in the pristine monolayer.

Among these functionalities, the formation of one-dimensional (1D) metallic channels along specific GBs—particularly mirror twin boundaries—is especially intriguing.[12–15] In MoS_2 and related TMDCs, such 1D metallic states have been directly observed using scanning tunnelling spectroscopy and photoemission spectroscopy,[13,16–18] and, more recently, through direct transport measurements along individual grain boundaries.[19] These states are of both fundamental and practical interest: they provide opportunities for realizing quantum wires, nanoscale interconnects, and catalytically active sites embedded within a semiconducting matrix.[20] Theoretically, their origin has been linked to discontinuities in the polarization vector across the boundary,[21–23] which give rise to delocalized, symmetry-protected conduction channels.[24]

However, despite these promising characteristics, the metallic behaviour of grain boundaries remains insufficiently understood. Many GBs that are predicted to be metallic exhibit instability toward spontaneous Peierls-like distortions[25] or symmetry breaking,[26] which generate charge density waves[27–29] and open a bandgap. Experimentally, GB conductivity is highly sensitive to growth conditions, local strain, doping, and chemical environment.[30,31] In particular, chalcogen vacancies—among the most prevalent native defects in MoS_2—can locally modify bonding environments and transport properties,[19,31–36] yet their specific influence on GB metallic states has not been systematically explored. Moreover, the role of chemical functionalization, such as hydrogen adsorption, remains largely unaddressed, despite its potential to alter defect energetics and passivate mid-gap states.[36–38] An in-depth understanding of how point defects and chemical

[a]*Institute of High Performance Computing (IHPC), Agency for Science, Technology and Research (A*STAR), 1 Fusionopolis Way, #16-16 Connexis, Singapore 138632, Republic of Singapore. E-mail: zhouhb@a-star.edu.sg, zhangyw@a-star.edu.sg*
[b]*Department of Electrical and Computer Engineering, National University of Singapore, 4 Engineering Drive 3, Singapore 117583, Republic of Singapore*
[c]*Institute of Materials Research and Engineering, Agency for Science, Technology and Research (A*STAR), 2 Fusionopolis Way, Singapore 138634, Republic of Singapore*

functionalization modulate the electronic properties of GBs is therefore essential for controlling 1D metallic states and for developing stable, functional grain boundary channels in 2D semiconductors.

In this work, we employ first-principles-based density functional theory (DFT) calculations to systematically investigate the impact of point defects and saturated hydrogenation on the electronic properties of representative mirror twin GBs in monolayer MoS_2. It is worth noting that MoS_2 exists in multiple structural polymorphs, including the 2H and 1T′ phases. While the present study focuses on the 2H phase due to its thermodynamic stability and widespread use in semiconducting applications, the 1T′ phase may exhibit distinct grain boundary structures and defect dynamics due to its distorted lattice and electronic properties.[39–41] Future work comparing the GB chemistry and defect energetics across different MoS_2 polymorphs, particularly under hydrogenation, could further elucidate structure–property relationships in these systems. We analyse how intrinsic defects and subsequent hydrogenation modulate the electronic band structures of mirror twin GBs. Our results show that the experimentally observed GBs exhibit a pronounced metal-to-semiconductor transition upon the introduction of point defects. In contrast, we predict two previously unexplored zigzag-bridging GBs that retain their metallic character and are robust against point-defect perturbations. Remarkably, hydrogenation exerts an opposite influence depending on the defect sensitivity of the GBs: for defect-sensitive GBs, hydrogenation can restore their metallic states; conversely, for defect-tolerant GBs, hydrogenation can induce a metal-to-semiconductor transition. This reversible behaviour is rooted in the redistribution of charge carriers at the GB core, demonstrating a compensatory mechanism between defect-induced localization and hydrogenation-induced screening.

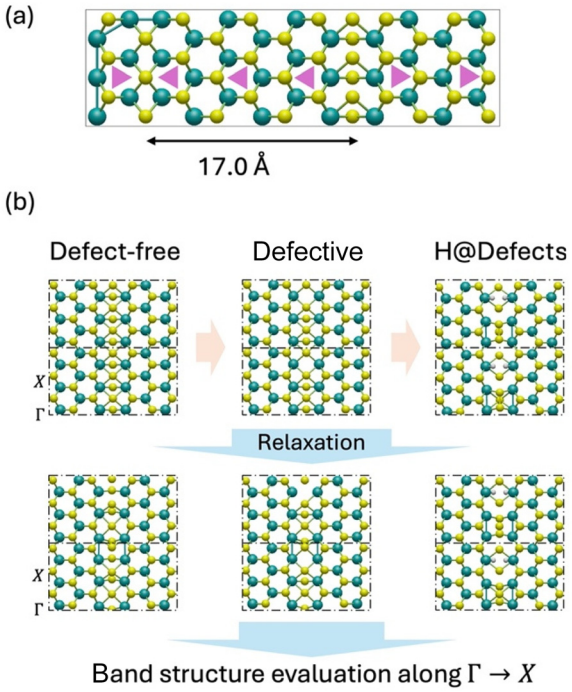

Fig. 1 (a) Top view of the integral supercell containing two mirror-symmetric grain boundaries in parallel separated by 17 Å. The total size of the simulation cell is 33.4 × 9.4 × 18 Å^3. (b) Simulation workflow for studying the effects of defects and hydrogenation on grain boundaries (GBs) in monolayer MoS_2, where the S-linked GB is used as an example. An ideal GB structure is first constructed and relaxed, and its electronic properties are assessed (first column). Point defects are then introduced, and the resulting structures are optimized and analysed (second column). Finally, hydrogen atoms are added at defect sites, and the passivated systems are further optimized to evaluate the impact on electronic behaviour (third column).

Model and methods

Fig. 1(a) shows a representative unit cell used in our calculation, featuring sulphur-linked (S-linked) and 4|4P GB grain boundaries in parallel. To model periodic systems, supercells containing two mirror-image GBs were constructed, with a separation of at least 15 Å to minimize interactions between the two GBs. We have carefully tested multiple GB–GB separations and found 15 Å to be sufficient to eliminate interactions between adjacent boundaries, as verified by the convergence of the electronic structure. As illustrated in Fig. 1(a), each pristine 2H-MoS_2 domain exhibits a built-in in-plane polarization along the armchair direction due to the lack of inversion symmetry. This polarization direction is indicated by the purple triangle in each domain. When two mirror-symmetric domains merge during growth, the polarization vectors point in opposite directions, resulting in a polarization mismatch at the grain boundary. This discontinuity arises intrinsically from the crystallographic orientation difference and has been observed in inversion domain boundaries formed during CVD growth.[3,7,31]

The simulation workflow is illustrated in Fig. 1(b), which outlines the computational procedure applied to selected GBs. A sulphur-linked GB structure, which has been predicted to be metallic in its defect-free form,[42,43] is used as an example. After the GB model was constructed, full structural relaxation was performed using density functional theory (DFT) calculations. Certain GBs, including the S-linked example, exhibited spontaneous trimerization during relaxation. The conduction characteristics of the relaxed structures were evaluated by calculating their electronic band structures, where the presence of a dispersive band crossing the Fermi level indicated metallic behaviour, while the opening of a bandgap at the Fermi level signified a semiconducting state.

Following the confirmation of the conduction type of defect-free GBs, the effects of point defects were investigated, as illustrated in the second column of Fig. 1(b). A single-point intrinsic defect was introduced at each GB per unit cell, corresponding to an overall defect concentration of around 2%. Three types of intrinsic defects were considered: single sulphur vacancies (S-vacancy), single molybdenum vacancies (Mo-vacancy) and double sulphur vacancies (2S-vacancy), reflecting the dominant vacancy types during the GB for-

mation. Following defect introduction, all structures were fully optimized, and their electronic properties were calculated.

To further explore the chemical modulation of the GB electronic properties, hydrogenation was introduced. Hydrogen atoms were relaxed to the most energetically favourable binding configurations. The optimized equilibrium electronic structures were subsequently analysed to determine the impact of hydrogenation on the conduction properties.

This systematic approach enables a comprehensive evaluation of how intrinsic defects and chemical functionalization collectively influence the electronic properties of grain boundaries.

Computationally, first-principles DFT calculations were performed using the Vienna *ab initio* simulation package (VASP).[44] The Perdew–Burke–Ernzerhof (PBE) functional[45] with generalized gradient approximation (GGA) was employed to consider the exchange–correlation effects. Projector augmented-wave (PAW) pseudopotentials[46] with a plane-wave energy cutoff of 520 eV were used throughout. Structural optimization was carried out for both atomic positions and lattice parameters until residual atomic forces were below 20 meV $Å^{-1}$. Electronic structure calculations were performed using a convergence criterion of 10^{-3} eV for total energy minimization. The Brillouin zone was sampled using a 6 × 2 × 1 Monkhorst–Pack *k*-point mesh[47] to ensure accurate electronic structure calculations. Atomic projected band structure analyses were performed to distinguish the electronic states originating from each GB. In addition, carrier localization behaviour was characterized by examining the Fermi velocity and the spatial distribution of electronic states near the Fermi level.

Results and discussion

Defect sensitivity of grain boundary conductivity

Mirror twin GBs in monolayer MoS_2 are capable of hosting one-dimensional (1D) metallic channels, but their stability is affected by intrinsic point defects and remains poorly understood. Building on our computational framework, we now systematically assess the defect sensitivity of representative GBs by introducing vacancy-type defects and evaluating their impact on electronic structure and conduction characteristics.

Defect sensitivity of observed GBs

Fig. 2 shows the relaxed atomic configuration and electronic band structures of three GB types widely studied in monolayer MoS_2: 4|4P, S-linked GB, and 4|8.[42,43] The metallic states of 4|4P and S-linked GBs in their defect-free forms have been predicted using previous simulations.[22,27,48,49] As shown in Fig. 2(a), the 4|4P GB retains metallic states after relaxation, consistent with previous studies,[22,23] attributed to strong bonding and effective electron transfer with the bulk lattice.[50] However, upon introducing a single sulphur vacancy or molybdenum vacancy, a bandgap opens near the Fermi level, with gap energies of 0.20 eV and 0.34 eV, respectively, indicating a transition from metallic to n-type semiconducting behaviour. This transition can be explained by the breaking of the C_{3h} symmetry,[21,26] which triples the lattice periodicity in the direction along the GB, relaxes the polarization discontinuity, and localizes the extended boundary states.[50] In contrast, when a double sulphur vacancy is introduced, the metallic character is preserved, which is attributed to the formation of Mo–Mo bonds across the vacancy site, preserving the conductive path as shown in Fig. 2(a).

Fig. 2(b) shows the electronic structure of the S-linked GBs. In the defect-free form, spontaneous trimerization triggers a metal-to-semiconductor transition, resulting in a direct bandgap of 0.88 eV. Upon introducing a single sulphur vacancy, the bandgap remains substantial, slightly decreasing to 0.76 eV. The gap reduces more significantly to 0.25 eV when a molybdenum vacancy is introduced. In the case of a double sulphur vacancy, the direct gap is converted into an indirect gap of 0.19 eV, with the conduction band minimum (CBM) located at the Γ point and the valence band minimum (VBM) at the *X* point, due to local atomic distortion.

Fig. 2(c) shows the electronic structure of the 4|8 GB, which exhibits an initial bandgap of 0.14 eV between the CBM and the defect-induced states, consistent with previous theoretical predictions.[10,51] Upon introducing different types of point defects, the gaps slightly increase to 0.17 eV, 0.16 eV and 0.21 eV for sulphur vacancies, molybdenum vacancies and double sulphur vacancies, respectively. These results indicate that the semiconducting properties of the 4|8 GB are robust against intrinsic point defects, implying stability of its electronic properties and potentially enhancing reliability for semiconductor device applications.

The calculated bandgaps for various GB types and defect configurations are summarized in Fig. 3. The inherent instability of the one-dimensional conductive channel, previously attributed to charge density formation *via* spontaneous trimerization,[16,27,50] is further corroborated by the defect-induced disruption observed in this study. Overall, metallic GBs exhibit sensitivity to perturbations and a tendency to transform into semiconducting states.

Defect tolerance of metallic S–S and Mo–Mo bridging GBs

The mirror twin GBs analysed above can be considered as connections of zigzag edges linked by either sulphur or molybdenum atoms. In addition to such configurations, we also examine another type of mirror twin GBs, which are formed by directly bridging the zigzag edges through S–S bonds or Mo–Mo bonds. We refer to these types of GBs as S–S bridging GBs and Mo–Mo bridging GBs, respectively. Their atomic structures are shown in Fig. 4. The defect-free forms of these structures have previously been predicted to be stable and metallic.[50] Here, we investigate the effects of intrinsic point defects on these two types of GBs. The calculated band structures are shown in Fig. 4. We find that both S–S and Mo–Mo bridging GBs demonstrate significant resilience to the effects of vacancies. Upon introducing either sulphur or molybdenum vacancies, these GBs retain their metallic nature. This behaviour can be attributed to the structure of the grain boundary,

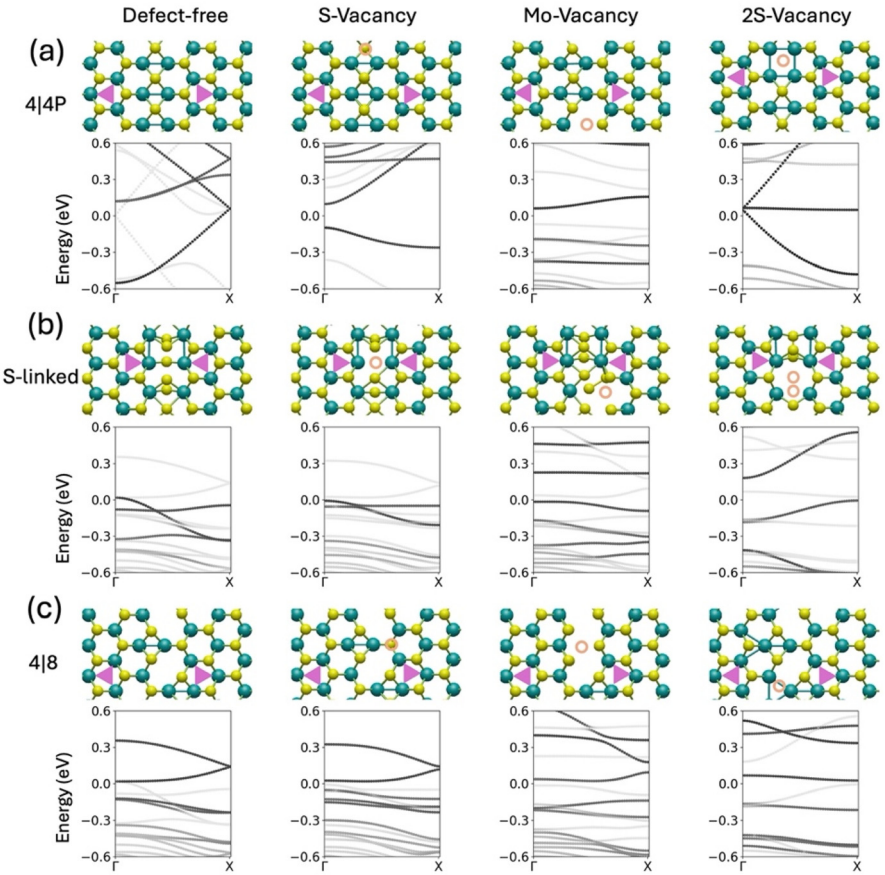

Fig. 2 Atomic configurations and band structures for three representative GBs: (a) 4|4P, (b) S-linked GB and (c) 4|8, under different defect configurations. Each column corresponds to one type of defect: defect-free, S vacancy, Mo vacancy, and double sulphur vacancy (2S-vacancy) at the GB centre. The Γ-X path is plotted for all the cases. The orange circle is plotted as a guide for the eye at the position of defects and the triangles emphasize the orientation of the bulk domains. The atomic configurations are fully relaxed. The Fermi levels are shifted to 0 in the band structure plots.

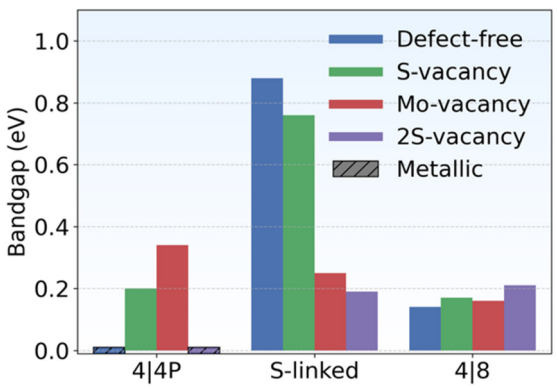

Fig. 3 Bandgaps of representative mirror twin grain boundaries (4|4P, S-linked, and 4|8) under different defect conditions—defect-free, single sulphur vacancy, single molybdenum vacancy, and double sulphur vacancy—plotted from left to right for each GB.

which comprises two parallel conductive pathways originating from the two parallel zigzag boundaries of each domain. The perturbation induced by a single vacancy on one domain exhibits a spatially limited impact on the symmetry and electronic structure of the opposing domain. Consequently, the overall electronic conductivity of the interface is largely preserved, rendering these GBs robust against point defects.

Although both types of GBs exhibit metallic behaviour even after defect introduction, they respond to defects differently. For S–S bridging GBs, as illustrated in Fig. 4(a), the introduction of a sulphur vacancy shifts the conduction band crossings with the Fermi level towards the Γ point. This suggests that longer-wavelength electronic states dominate the transport, rendering the conduction less sensitive to local defects. In Mo–Mo bridging GBs, as shown in Fig. 4(b), molybdenum vacancies induce a diminished band dispersion and an accompanying reduction in the number of conducting channels. Specifically, the defect-free GB exhibits two metallic bands, whereas the introduction of a single molybdenum vacancy results in the disappearance of one of these bands, signifying the disruption of a conducting pathway. These observations indicate that the presence of dual, spatially separated parallel conduction paths can offset local perturbations, thereby enhancing the robustness of the metallic behaviour. The persistence of metallic conduction in these GBs, even in the pres-

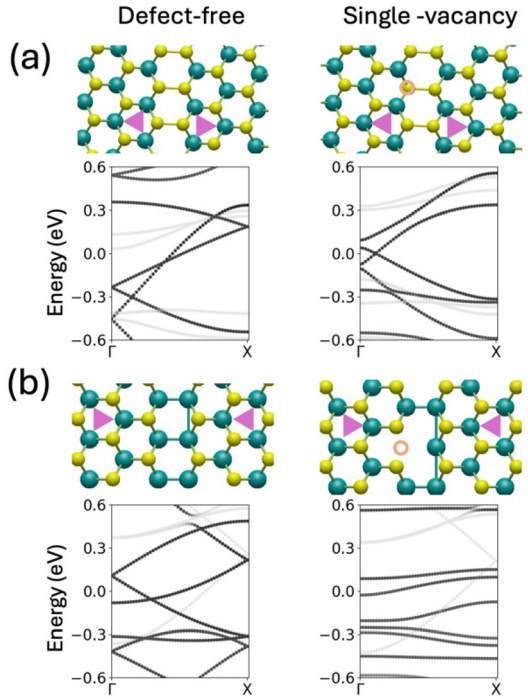

Fig. 4 Fully relaxed atomic configurations of (a) S–S bridging and (b) Mo–Mo bridging GBs, for defect-free structures (left column) and structures with single defects (right column). Single sulphur vacancies are introduced into the S–S bridging GB while single Mo vacancies are introduced into the Mo–Mo bridging GB. The orange circle is plotted as a guide for the eye at the position of defects and the triangles represent the orientation of the bulk domains. The Fermi levels are aligned to 0 in all band structure plots.

ence of structural perturbations, suggests a deeper underlying origin. A mechanism for the topological polarization discontinuities between adjacent domains in hexagonal boron nitride (h-BN) has been proposed by Jung *et al.*,[52] where conducting graphene nanoroads embedded in BN sheets emerge due to a change in the topological index across the interface. A recent theoretical work by Krishnamurthi and Brocks has demonstrated that certain one-dimensional metallic states in TMDC grain boundaries also arise from topological polarization discontinuities between adjacent domains.[49] Drawing from these insights, the robust metallic states observed in GBs such as Mo–Mo and S–S bridging structures may likewise be attributed to topologically protected boundary modes stemming from underlying polarization or symmetry discontinuities. This inherent defect tolerance is crucial for ensuring reliable electronic transport in realistic device operating conditions, where the presence of atomic-scale defects is unavoidable.

The formation energy of grain boundaries and defects

To assess the thermodynamic favourability of vacancy formation at grain boundaries, we calculated the formation energies for selected GBs in both defect-free and defective forms, following the methodology outlined in ref. 53 and 54. The formation energy is defined as $(E_{tot} - N_S E_{S\_ML} - N_{Mo} E_{Mo\_ML})/2L$, where L is the length of the GBs, E_{tot} is the total energy of the system, and E_{S_ML} and E_{Mo_ML} are the reference energies of S and Mo atoms in a pristine MoS_2 monolayer, respectively. These energies are computed as $E_{S\_ML} = E_S^0 + E_{bond}$ and $E_{Mo\_ML} = E_{Mo}^0 + 2E_{bond}$. The bond energy is derived from $E_{bond} = [E_{uc} - E_{Mo}^0 - 2E_S{}^0]/4$, where E_{Mo}^0 and E_S^0 are the energies of Mo and S atoms in their solid phases, respectively. Here, E_{uc} is the energy of the unit cell of a pristine MoS_2 monolayer. The results, shown in Fig. 5, reveal a broad range of thermodynamic stabilities.

Among the structures considered, the Mo–Mo bridging and 4|4P GB combinations exhibit the lowest formation energy (0.83 eV nm^{-1}), making them the most energetically favourable GB configurations. Notably, these low-energy GBs maintain metallic states in their defect-free form. Conversely, semiconductor GBs, such as the S-linked and 4|8 configurations, possess significantly higher formation energies (5.7 eV nm^{-1}), suggesting they are more likely to form under constrained or non-equilibrium conditions.

Fig. 5 also shows that defect introduction affects the GB stabilities. Sulphur vacancies are generally more favourable than molybdenum vacancies, as reflected by their lower formation energy. Specifically, in the S-linked and S–S bridging GBs, the formation of sulphur vacancies results in a reduction of the total formation energy by 0.48 eV nm^{-1} and 0.37 eV nm^{-1}, respectively. This energetic favourability suggests a thermodynamic driving force for the spontaneous formation of such vacancies *via* structural reconstruction. Meanwhile, molybdenum vacancies substantially increase the formation energy in all cases, consistent with their limited presence in experimental samples.[55,56] Interestingly, the formation energies for the double sulphur vacancy in S-linked, 4|4P and 4|8 GBs remain within 5% of their defect-free counterparts, implying that certain complex vacancy configurations may be more stable than expected. Overall, the formation energies for all defect types remain relatively low and experimentally accessible, highlighting the importance of defect analysis for understanding both the electronic behaviour and the thermodynamic stability of grain boundaries.

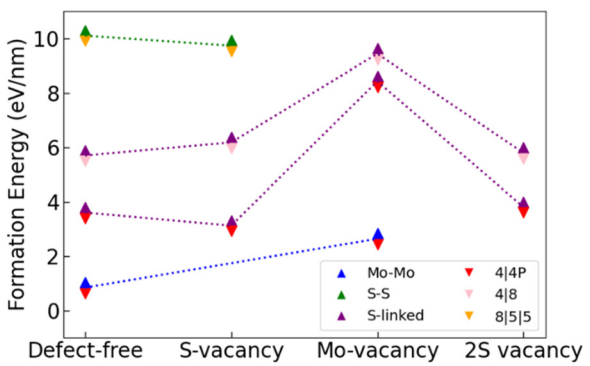

Fig. 5 Formation energies of different grain boundaries and their defective forms, with formation energy of two GBs evaluated simultaneously within each unit cell.

Hydrogenation enables reversible control of metallicity

Hydrogenation offers an additional strategy for tuning the electronic properties of grain boundaries by saturating bonds introduced by intrinsic defects. To systematically investigate this influence, we examine the effects of hydrogen atoms, introduced at the defect sites, on the electrical conductivity of mirror twin GBs that contain defects. Specifically, we focus on whether hydrogenation can restore the metallic states of GBs that have undergone defect-induced metal-to-semiconductor transitions, as well as its impact on defect-tolerant metallic GBs.

Hydrogen-induced recovery of metallic behaviour in defect-sensitive GBs

Fig. 6 shows the atomic configurations and corresponding band structures after hydrogenation at the single-vacancy sites for the semiconducting GBs: 4|4P, S-linked and 4|8. Strikingly, all three types of GBs exhibit band crossing at the Fermi level, indicating that the defect-induced bandgaps previously predicted (as shown in Fig. 2) have been eliminated.

Specifically, the 4|4P GB shows clear dispersive conducting bands after hydrogenation, closing the defect-induced bandgap (Fig. 6(a)). This behaviour implies that the loss of metallic states due to defect introduction can be effectively recovered. From a theoretical standpoint, this is plausible since hydrogenation introduces electrons into the electronic system while minimally perturbing the elastic restoring forces governing atomic displacements. Previous analyses have shown that the metallic state of GBs is highly sensitive to the charge transfer at the boundary atoms when interatomic force constants are held fixed.[50] This finding is particularly important because 4|4P is one of the most frequently formed GBs. It is a promising candidate for one-dimensional conducting chain applications, exhibiting low formation energy in both its defect-free and sulphur-vacancy forms. Hydrogenation thus offers a promising pathway to suppress the degradation of metallic states resulting from unavoidable sulphur vacancies and to improve the robustness of the conductive channels.

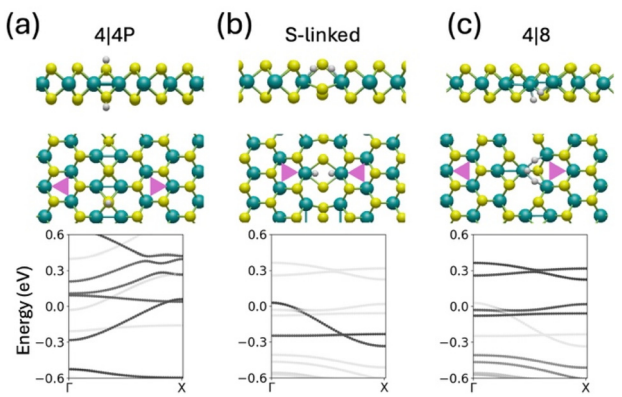

Fig. 6 Fully relaxed atomic configuration of GBs with hydrogenation at the position of point defects. Three semiconducting types of GBs are investigated: (a) 4|4P, (b) S-linked GB and (c) 4|8 with single sulphur vacancies. The Fermi levels are aligned to 0 in all band structure plots. The side view and top view are provided for clear observation of the positions of the hydrogen atoms.

Fig. 6(b) shows the electronic properties of S-linked GBs after hydrogenation. A conducting band appears, and the system exhibits metallic behaviour. Relative to the defect-free states in Fig. 2(b), the conducting band appears due to a downward Fermi level shift, which moves the previously occupied valence band into the conduction region and makes it dispersive. This shift indicates electron injection by the hydrogen atoms, which alters the electron density distribution and leads to the presence of excess carriers responsible for the conduction. This behaviour is consistent with the conductivity phase domain model introduced in previous studies,[50] where hydrogenation modified the charge transfer equilibrium between the GB and the surrounding 2D domains, thereby promoting electronic delocalization.

Similarly, Fig. 6(c) shows the emergence of dispersive bands in the 4|8 GB after hydrogenation, reverting the previous semiconducting states to a metallic one. In this case, three hydrogen atoms are located at a defect site. The resulting dispersive bands lie near the Fermi level and appear flat in momentum space, implying their origin from defect states. To determine the spatial extent of these defect states, we calculated the Fermi velocity using the formula $v_F = \frac{1}{\hbar}\frac{dE}{dk}$ and found it to be 5.7×10^4 m s^{-1}. This value, while lower than that of typical metals,[57] is significantly non-zero, indicating extended states. This suggests that conduction occurs *via* extended defect states characterized by weak wavefunction overlap between mid-gap metallic modes,[15] creating channels for electrons to hop along the defect network.[58] Such one-dimensional hopping channels could exhibit strong electron correlations, potentially leading to enhanced thermoelectric performance *via* strong Seebeck effects.[59]

Our results demonstrate that hydrogenation can effectively restore the metallic states of GBs that have undergone either spontaneous trimerization or defect-induced metal-to-semiconductor transitions. This indicates that hydrogenation offers reversible control over the electronic properties of GBs. These findings could guide experimental efforts in fabricating robust one-dimensional metallic wires resistant to local perturbations.

Metal-to-semiconductor transition in robust grain boundaries

Fig. 7 shows the effects of hydrogenation on GBs that are otherwise robust against point defects: S–S and Mo–Mo bridging GBs. Unexpectedly, these GBs undergo a transition upon hydrogenation, shifting from metallic to semiconducting states.

For the S–S bridging GB, as shown in Fig. 7(a), a small direct bandgap of 0.11 eV is observed at the middle point along the Γ–X path. This transition can be attributed to hydrogen-induced charge redistribution. Despite the structural robustness of parallel zigzag edge GBs against unilateral atomic defects, they remain susceptible to perturbations from the local electronic environment. Hydrogen atoms, by altering the local electrostatic potential and disrupting the subtle sym-

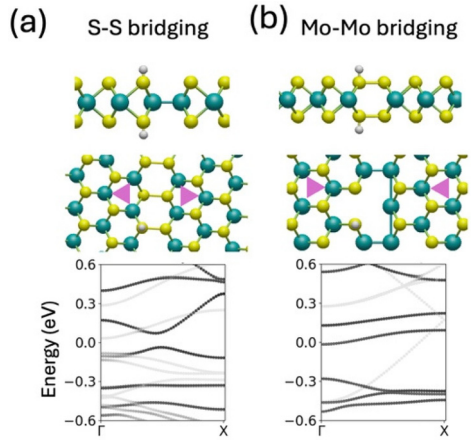

Fig. 7 Fully relaxed atomic configuration of GBs with hydrogenation at the position of point defects. Two metallic types of GBs are investigated: (a) S–S bridging GB with single sulphur vacancies and (b) Mo–Mo bridging GB with single Mo vacancies. The Fermi levels are aligned to 0 in all band structure plots. The side view and top view are provided for clear observation of the positions of the hydrogen atoms.

metry of the bonding network, effectively localize the electronic states near defect sites. Despite structural stability, these GBs exhibit electronic instability and gap formation under local charge perturbations.

For the Mo–Mo bridging GB, as shown in Fig. 7(b), an n-type bandgap of 0.26 eV forms at the Γ point. Although a minor crossing of the conduction band near the Γ point is observed, this state exhibits a very low Fermi velocity of 4.6×10^3 m s^{-1} and it is effectively localized. The opening of a bandgap in these otherwise defect-robust GBs highlights the dual role of hydrogenation: while it can restore metallic states in defect-sensitive boundaries, it can also induce new electronic transitions in structurally robust GBs by modifying the local charge distribution. This finding underscores the critical sensitivity of GB electronic properties to the local chemical environment.

Fig. 8 quantitatively illustrates the reversible conductivity modulation by hydrogenation, showing the band gaps of the

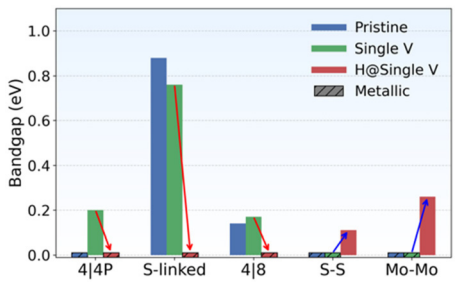

Fig. 8 Bandgaps of various grain boundaries under three structural conditions—defect-free, single-defective and hydrogenated—plotted from left to right for each GB. Red arrows show the restoration of metallicity by hydrogenation, while the blue arrows show bandgap opening by hydrogenation.

five GB types across defect-free, defective and hydrogenated states. It is seen that while defects may alter the conductivity differently across various GBs, hydrogenation consistently reverses the conductivity relative to the defective states, as indicated by the red and blue arrows.

To further assess the robustness of these trends, we performed additional calculations using spin-polarized and hybrid functional approaches. These complementary approaches allow us to evaluate the sensitivity of our results to the inclusion of spin degrees of freedom and the choice of the exchange–correlation functional, which are particularly relevant in systems with dangling bonds or unsaturated defects.

We first carried out spin-polarized calculations for two representative GB types: the 4|4P GB and the Mo–Mo bridging GB. The 4|4P GB, which undergoes a metal-to-semiconductor transition upon introduction of a sulphur vacancy, reverts to metallic conductivity upon hydrogenation—consistent with our spin-unpolarized results. In the S-vacancy case, a slight reduction in the bandgap is observed, from 0.20 eV (unpolarized) to 0.16 eV (spin-polarized). Spin splitting appears only in the hydrogenated configuration, while the defect-free and S-vacancy structures remain spin-degenerate. For the Mo–Mo bridging GB, the metallic state remains robust in the Mo-vacancy case, but hydrogenation induces a bandgap opening. This gap is slightly reduced from 0.26 eV in the spin-unpolarized case to 0.22 eV with spin polarization. These results indicate that while spin polarization can slightly shift the band edges and induce splitting in specific cases, it does not qualitatively alter the electronic character of the GBs. The corresponding spin-resolved band structures are provided in Fig. S1.

To further validate the bandgap predictions, we conducted hybrid-functional calculations using the HSE06 functional with 25% Hartree–Fock exchange. Due to computational cost, a reduced K-point mesh (11 points) was used. The HSE results are provided in Fig. S2. Across all six cases—defect-free, vacancy, and hydrogenated structures for both GB types—we find that the semiconducting or metallic nature is consistent with the PBE results. Quantitatively, for the 4|4P GB with a sulphur vacancy, the gap increases from 0.20 eV (PBE) to 0.26 eV (HSE), while the hydrogenated case remains metallic under both functionals. For the Mo–Mo bridging GB, the hydrogenated structure exhibits a bandgap of 0.26 eV (PBE) and 0.23 eV (HSE), with the defect-free and vacancy cases remaining metallic. These comparisons demonstrate that both spin and hybrid-functional treatments corroborate the robustness of our findings.

Together, these additional analyses reinforce the reliability of our PBE-based conclusions and highlight a compensatory relationship between defect-induced gap opening and hydrogen-induced metallicity restoration. This opposing effect suggests that defect engineering and hydrogenation represent two controllable and reversible strategies for tuning GB conductivity. Moreover, the sensitivity of GB electronic states to charge perturbations implies that other external stimuli, such as doping or chemical functionalization, may offer further avenues for modulating the bandgap and conductivity in 2D polycrystalline materials.

Conclusion

Our first-principles study reveals the contrasting effects of vacancies and hydrogenation on the electronic properties of representative mirror twin grain boundaries in MoS_2. We demonstrate a reversible tuning of grain boundary conduction through opposing mechanisms: defect engineering and hydrogenation. In defect-sensitive boundaries, vacancies induce band gaps and suppress metallicity, while hydrogenation can recover metallic states by defect passivation. Conversely, defect-robust boundaries retain metallic states despite vacancies, but hydrogenation can induce gap formation, rendering them semiconducting. This dual and opposing tunability provides a reversible and controllable strategy for engineering grain boundary transport in two-dimensional semiconductors.

Conflicts of interest

There are no conflicts to declare.

Data availability

The software used for density functional theory simulation is VASP.[44] Theoretical crystallographic data for MoS_2 GBs have been deposited at the CCDC under 2454045–2454053.

Spin-polarized calculation and hybrid functional calculation (HSE06) are available in the Supplementary information. See DOI: **https://doi.org/10.1039/d5nr02232k**.

CCDC 2454045–2454053 contain the supplementary crystallographic data for this paper.[60a–i]

Acknowledgements

This work was supported by the National Research Foundation, Singapore, under Award No. NRF-CRP24-2020-0002. Y.-W. Z. acknowledges support from the Singapore A*STAR SERC CRF Award. The use of computing resources at the A*STAR Computational Centre and National Supercomputer Centre, Singapore, is gratefully acknowledged.

References

1 T. Severs Millard, A. Genco, E. M. Alexeev, S. Randerson, S. Ahn, A.-R. Jang, H. Shin and A. I. Tartakovskii, *npj 2D Mater. Appl.*, 2020, **4**, 1–9.
2 T. H. Ly, M.-H. Chiu, M.-Y. Li, J. Zhao, D. J. Perello, M. O. Cichocka, H. M. Oh, S. H. Chae, H. Y. Jeong, F. Yao, L.-J. Li and Y. H. Lee, *ACS Nano*, 2014, **8**, 11401–11408.
3 A. M. Van Der Zande, P. Y. Huang, D. A. Chenet, T. C. Berkelbach, Y. You, G.-H. Lee, T. F. Heinz, D. R. Reichman, D. A. Muller and J. C. Hone, *Nat. Mater.*, 2013, **12**, 554–561.
4 Y. Shi, M. Rabbani, Á. Vázquez-Mayagoitia, J. Zhao and W. A. Saidi, *Nanoscale*, 2022, **14**, 617–625.
5 J. Shen, A. Aljarb, Y. Cai, X. Liu, J. Min, Y. Wang, Q. Wang, C. Zhang, C. Chen, M. Hakami, J.-H. Fu, H. Zhang, G. Li, X. Wang, Z. Chen, J. Li, X. Dong, K. Shih, K.-W. Huang, V. Tung, G. Shi, I. Pinnau, L.-J. Li and Y. Han, *Science*, 2025, **387**, 776–782.
6 Y. He, P. Tang, Z. Hu, Q. He, C. Zhu, L. Wang, Q. Zeng, P. Golani, G. Gao, W. Fu, Z. Huang, C. Gao, J. Xia, X. Wang, X. Wang, C. Zhu, Q. M. Ramasse, A. Zhang, B. An, Y. Zhang, S. Martí-Sánchez, J. R. Morante, L. Wang, B. K. Tay, B. I. Yakobson, A. Trampert, H. Zhang, M. Wu, Q. J. Wang, J. Arbiol and Z. Liu, *Nat. Commun.*, 2020, **11**, 57.
7 T. H. Ly, D. J. Perello, J. Zhao, Q. Deng, H. Kim, G. H. Han, S. H. Chae, H. Y. Jeong and Y. H. Lee, *Nat. Commun.*, 2016, **7**, 10426.
8 K. Xu, T. Liang, Z. Zhang, X. Cao, M. Han, N. Wei and J. Wu, *Nanoscale*, 2022, **14**, 1241–1249.
9 X. Liu, Z. G. Yu, G. Zhang and Y.-W. Zhang, *Nanoscale*, 2020, **12**, 17746–17753.
10 V. Sorkin, H. Zhou, Z. G. Yu, K.-W. Ang and Y.-W. Zhang, *Phys. Chem. Chem. Phys.*, 2025, **27**, 905–914.
11 H. Zhou, Z.-Y. Ong, G. Zhang and Y.-W. Zhang, *Nanoscale*, 2022, **14**, 9209–9217.
12 Q. D. Truong, N. T. Hung, Y. Nakayasu, K. Nayuki, Y. Sasaki, D. M. Kempaiah, L.-C. Yin, T. Tomai, R. Saito and I. Honma, *RSC Adv.*, 2018, **8**, 33391–33397.
13 Y. Ma, S. Kolekar, H. Coy Diaz, J. Aprojanz, I. Miccoli, C. Tegenkamp and M. Batzill, *ACS Nano*, 2017, **11**, 5130–5139.
14 M. V. Bollinger, J. V. Lauritsen, K. W. Jacobsen, J. K. Nørskov, S. Helveg and F. Besenbacher, *Phys. Rev. Lett.*, 2001, **87**, 196803.
15 H. Liu, L. Jiao, F. Yang, Y. Cai, X. Wu, W. Ho, C. Gao, J. Jia, N. Wang, H. Fan, W. Yao and M. Xie, *Phys. Rev. Lett.*, 2014, **113**, 066105.
16 Y. Ma, H. C. Diaz, J. Avila, C. Chen, V. Kalappattil, R. Das, M.-H. Phan, T. Čadež, J. M. P. Carmelo, M. C. Asensio and M. Batzill, *Nat. Commun.*, 2017, **8**, 14231.
17 C. Yan, X. Dong, C. H. Li and L. Li, *Nanotechnology*, 2018, **29**, 195704.
18 H. W. Kim, *Appl. Microsc.*, 2023, **53**, 5.
19 B. Deng, H. Ahn, J. Wang, G. Moon, C. Han, N. Dongre, C. Lei, G. Scuri, J. Sung, E. Brutschea, K. Watanabe, T. Taniguchi, F. Zhang, M.-H. Jo and H. Park, *Phys. Rev. Lett.*, 2025, **134**, 046301.
20 Y.-C. Lin, D. O. Dumcenco, Y.-S. Huang and K. Suenaga, *Nat. Nanotechnol.*, 2014, **9**, 391–396.
21 N. C. Bristowe, M. Stengel, P. B. Littlewood, E. Artacho and J. M. Pruneda, *Phys. Rev. B:Condens. Matter Mater. Phys.*, 2013, **88**, 161411.
22 S. Zhang, B. Huang, Y. Dai and W. Wei, *Comput. Mater. Sci.*, 2022, **203**, 111115.
23 M. Gibertini and N. Marzari, *Nano Lett.*, 2015, **15**, 6229–6238.
24 S. Krishnamurthi and G. Brocks, *npj 2D Mater. Appl.*, 2021, **5**, 1–6.

25 S. Krishnamurthi, M. Farmanbar and G. Brocks, *Phys. Rev. B*, 2020, **102**, 165142.
26 P. Jadaun, D. Xiao, Q. Niu and S. K. Banerjee, *Phys. Rev. B: Condens. Matter Mater. Phys.*, 2013, **88**, 085110.
27 S. Barja, S. Wickenburg, Z.-F. Liu, Y. Zhang, H. Ryu, M. M. Ugeda, Z. Hussain, Z.-X. Shen, S.-K. Mo, E. Wong, M. B. Salmeron, F. Wang, M. F. Crommie, D. F. Ogletree, J. B. Neaton and A. Weber-Bargioni, *Nat. Phys.*, 2016, **12**, 751–756.
28 J.-H. Choi, S. Liu, W. Zhang, Z. Liu and M. H. Rummeli, *Small*, 2018, **14**, 1803040.
29 M. Batzill, *J. Phys.: Condens. Matter*, 2018, **30**, 493001.
30 J. Ludwig, A. N. Mehta, M. Mascaro, U. Celano, D. Chiappe, H. Bender, W. Vandervorst and K. Paredis, *Nanotechnology*, 2019, **30**, 285705.
31 J. Lin, S. T. Pantelides and W. Zhou, *ACS Nano*, 2015, **9**, 5189–5197.
32 S. Zhang, X. Wang, Y. Wang, H. Zhang, B. Huang, Y. Dai and W. Wei, *J. Phys. Chem. Lett.*, 2022, **13**, 4807–4814.
33 O. Lehtinen, H.-P. Komsa, A. Pulkin, M. B. Whitwick, M.-W. Chen, T. Lehnert, M. J. Mohn, O. V. Yazyev, A. Kis, U. Kaiser and A. V. Krasheninnikov, *ACS Nano*, 2015, **9**, 3274–3283.
34 J. Park, K.-H. Xue, M. Mouis, F. Triozon and A. Cresti, *Phys. Rev. B*, 2019, **100**, 235403.
35 H. Zhou, V. Sorkin, S. Chen, Z. Yu, K. Ang and Y. Zhang, *Adv. Electrode Mater.*, 2023, **9**, 2201252.
36 Y. Cai, H. Zhou, G. Zhang and Y.-W. Zhang, *Chem. Mater.*, 2016, **28**, 8611–8621.
37 Z. Li, H. Bretscher and A. Rao, *Nanoscale*, 2024, **16**, 9728–9741.
38 Y. Cai, Q. Ke, G. Zhang, Y. P. Feng, V. B. Shenoy and Y.-W. Zhang, *Adv. Funct. Mater.*, 2015, **25**, 2230–2236.
39 M. Kan, J. Y. Wang, X. W. Li, S. H. Zhang, Y. W. Li, Y. Kawazoe, Q. Sun and P. Jena, *J. Phys. Chem. C*, 2014, **118**, 1515–1522.
40 M. Precner, T. Polaković, Q. Qiao, D. J. Trainer, A. V. Putilov, C. Di Giorgio, I. Cone, Y. Zhu, X. X. Xi, M. Iavarone and G. Karapetrov, *Sci. Rep.*, 2018, **8**, 6724.
41 J. Zhu, Z.-C. Wang, H. Dai, Q. Wang, R. Yang, H. Yu, M. Liao, J. Zhang, W. Chen, Z. Wei, N. Li, L. Du, D. Shi, W. Wang, L. Zhang, Y. Jiang and G. Zhang, *Nat. Commun.*, 2019, **10**, 1348.
42 W. Zhou, X. Zou, S. Najmaei, Z. Liu, Y. Shi, J. Kong, J. Lou, P. M. Ajayan, B. I. Yakobson and J.-C. Idrobo, *Nano Lett.*, 2013, **13**, 2615–2622.
43 X. Zou, Y. Liu and B. I. Yakobson, *Nano Lett.*, 2013, **13**, 253–258.
44 G. Kresse and J. Furthmüller, *Phys. Rev. B:Condens. Matter Mater. Phys.*, 1996, **54**, 11169–11186.
45 J. P. Perdew, K. Burke and M. Ernzerhof, *Phys. Rev. Lett.*, 1996, **77**, 3865–3868.
46 P. E. Blöchl, *Phys. Rev. B:Condens. Matter Mater. Phys.*, 1994, **50**, 17953–17979.
47 H. J. Monkhorst and J. D. Pack, *Phys. Rev. B*, 1976, **13**, 5188–5192.
48 D. Le and T. S. Rahman, *J. Phys.: Condens. Matter*, 2013, **25**, 312201.
49 S. Krishnamurthi and G. Brocks, *Phys. Rev. B*, 2020, **102**, 161106.
50 H. Zhou, V. Sorkin, Z. Yu and Y.-W. Zhang, *J. Phys. Chem. C*, 2025, **129**, 670–676.
51 X. Qiu, Y. Wang and Y. Jiang, *Phys. Chem. Chem. Phys.*, 2021, **23**, 11937–11943.
52 J. Jung, Z. Qiao, Q. Niu and A. H. MacDonald, *Nano Lett.*, 2012, **12**, 2936–2940.
53 N. Gao, Y. Guo, S. Zhou, Y. Bai and J. Zhao, *J. Phys. Chem. C*, 2017, **121**, 12261–12269.
54 J. Hong, Z. Hu, M. Probert, K. Li, D. Lv, X. Yang, L. Gu, N. Mao, Q. Feng, L. Xie, J. Zhang, D. Wu, Z. Zhang, C. Jin, W. Ji, X. Zhang, J. Yuan and Z. Zhang, *Nat. Commun.*, 2015, **6**, 6293.
55 S. Helveg, J. V. Lauritsen, E. Lægsgaard, I. Stensgaard, J. K. Nørskov, B. S. Clausen, H. Topsøe and F. Besenbacher, *Phys. Rev. Lett.*, 2000, **84**, 951–954.
56 J. Hong, Y. Wang, A. Wang, D. Lv, C. Jin, Z. Xu, M. I. J. Probert, J. Yuan and Z. Zhang, *Nanoscale*, 2017, **9**, 10312–10320.
57 C. Kittel, *Introduction to Solid State Physics*, Wiley, 2004.
58 H. Qiu, T. Xu, Z. Wang, W. Ren, H. Nan, Z. Ni, Q. Chen, S. Yuan, F. Miao, F. Song, G. Long, Y. Shi, L. Sun, J. Wang and X. Wang, *Nat. Commun.*, 2013, **4**, 2642.
59 C. Wu, X.-L. Shi, L. Wang, W. Lyu, P. Yuan, L. Cheng, Z.-G. Chen and X. Yao, *ACS Nano*, 2024, **18**, 31660–31712.
60 (*a*) H. Zhou, V. Sorkin, Z. G. Yu, K.-W. Ang and Y.-W. Zhang, CCDC 2454045: Experimental Crystal Structure Determination, 2025, DOI: **10.5517/ccdc.csd.cc2ncmrf**; (*b*) H. Zhou, V. Sorkin, Z. G. Yu, K.-W. Ang and Y.-W. Zhang, CCDC 2454046: Experimental Crystal Structure Determination, 2025, DOI: **10.5517/ccdc.csd.cc2ncmsg**; (*c*) H. Zhou, V. Sorkin, Z. G. Yu, K.-W. Ang and Y.-W. Zhang, CCDC 2454047: Experimental Crystal Structure Determination, 2025, DOI: **10.5517/ccdc.csd.cc2ncmth**; (*d*) H. Zhou, V. Sorkin, Z. G. Yu, K.-W. Ang and Y.-W. Zhang, CCDC 2454048: Experimental Crystal Structure Determination, 2025, DOI: **10.5517/ccdc.csd.cc2ncmvj**; (*e*) H. Zhou, V. Sorkin, Z. G. Yu, K.-W. Ang and Y.-W. Zhang, CCDC 2454049: Experimental Crystal Structure Determination, 2025, DOI: **10.5517/ccdc.csd.cc2ncmwk**; (*f*) H. Zhou, V. Sorkin, Z. G. Yu, K.-W. Ang and Y.-W. Zhang, CCDC 2454050: Experimental Crystal Structure Determination, 2025, DOI: **10.5517/ccdc.csd.cc2ncmxl**; (*g*) H. Zhou, V. Sorkin, Z. G. Yu, K.-W. Ang and Y.-W. Zhang, CCDC 2454051: Experimental Crystal Structure Determination, 2025, DOI: **10.5517/ccdc.csd.cc2ncmym**; (*h*) H. Zhou, V. Sorkin, Z. G. Yu, K.-W. Ang and Y.-W. Zhang, CCDC 2454052: Experimental Crystal Structure Determination, 2025, DOI: **10.5517/ccdc.csd.cc2ncmzn**; (*i*) H. Zhou, V. Sorkin, Z. G. Yu, K.-W. Ang and Y.-W. Zhang, CCDC 2454053: Experimental Crystal Structure Determination, 2025, DOI: **10.5517/ccdc.csd.cc2ncn0q**.